





Cellular crosstalk mediated by TGF- β drives epithelial-mesenchymal transition in patient-derived multi-compartment biliary organoids

Received: 1 June 2024

Accepted: 21 June 2025

Published online: 17 July 2025

 Check for updates

Hiroaki Ayabe ¹, Erica A. K. DePasquale ², Surya P. Amarachintha³, Reena Mourya¹, Wenqi Li¹, Shreya Nalluri⁴, Sejal R. Fox⁵, Kenichiro Konishi^{2,6}, Pranavkumar Shivakumar ¹ ✉ & Jorge A. Bezerra ¹ ✉

Deficiencies in the development of epithelial structures and delays in cellular maturation can increase the susceptibility of neonates to disease early in life. To investigate human biliary development and its vulnerability to biliary atresia, a severe pediatric cholangiopathy, we engineered multi-compartment biliary organoids (MBOs) from co-cultures of human liver-derived epithelial organoid cells with human endothelial and mesenchymal cells. MBOs derived from normal livers effectively replicated the epithelial structure of the bile duct epithelium and peribiliary glands (PBGs). Conversely, MBOs from diseased livers exhibited defective epithelial layers, a significant epithelial-mesenchymal transition (EMT), and an activation of the TGF- β /Activin-SMAD2/3 signaling, primarily due to intermediary cell sub-populations. Inhibition of TGF- β signaling suppressed EMT and promoted biliary epithelial development in human MBOs and suppressed the phenotype of experimental biliary atresia in neonatal mice. Thus, the modulation of TGF- β -dependent EMT regulates bile duct epithelial development and influences the susceptibility of neonates to biliary injuries.

The normal development of epithelial compartments and functional cellular maturation are important for postnatal adaptation to extra-uterine life. There is increasing evidence that delayed maturation may render neonates susceptible to diseases, as evidenced by the time-restricted onset of biliary injury in neonates with biliary atresia (BA), a severe cholangiopathy of childhood. The biliary tract is composed of the gallbladder and bile ducts, with an epithelial lining that also contains peribiliary glands (PBGs) along the intra- (IHBD)

and extrahepatic bile ducts (EHBD)^{1,2}. Although the epithelial lining allows for an uninterrupted flow of bile into the duodenum, it has other physiological functions, such as mucin production and stem cell reservoir^{3,4}. Thus, biliary epithelial integrity is crucial in preventing hepatic and biliary diseases^{5–9}. Although several factors have been linked to the etiology of the disease, the mechanisms of epithelial disruption and the rapid progression of fibrosis remain undefined.

¹Department of Pediatrics, University of Texas Southwestern Medical Center and Children's Medical Center, Dallas, TX, USA. ²Division of Gastroenterology, Hepatology & Nutrition, Cincinnati Children's Hospital Medical Center, Cincinnati, OH, USA. ³Department of Biology, Georgia Southwestern State University, Americus, GA, USA. ⁴Graduate Program in Bioinformatics, Boston University Center for Computing and Data Sciences, Boston, MA, USA. ⁵Division of Experimental Hematology and Cancer Biology, Cincinnati Children's Hospital Medical Center, Cincinnati, OH, USA. ⁶Department of General-Pediatric Hepatobiliary Pancreatic Surgery, Kitasato University School of Medicine, Kanagawa, Japan. ✉ e-mail: Pranavkumar.Shivakumar@utsouthwestern.edu; Jorge.Bezerra@utsouthwestern.edu

Bile duct epithelial injury by the administration of rhesus rotavirus (RRV) to neonatal mice recapitulates the tissue injury observed in human neonates^{10–12}. However, the recovery of viruses from human BA tissues is inconsistent. The best evidence that the developmental defects play a significant role in the prenatal onset of disease emerged from the detection of hyperbilirubinemia within days of birth in newborn infants who later develop BA^{13–15}. Although harmful mutations in several genes, such as *PKD1L1*, *ADD3*, *EFEMP1*, *KIF3B*, *TTC17*, and *PCNT*, have been linked to abnormal bile duct development, these mutations are detected in only a small subset of patients^{16–18}.

Studies using patient-derived cholangiocyte organoids revealed a delayed maturation of epithelial cells, with altered tight junctions, functional defects, and mal-positioning of cilia^{19,20}. Based on these data, we hypothesized that the delayed maturation of the diseased biliary epithelium results from altered crosstalk between neighboring epithelial and mesenchymal cells. To test this hypothesis, we established human multi-compartment biliary organoids (MBOs) by coculturing cells from normal- and patient-derived cholangiocyte organoids with human umbilical vein endothelial cells (HUVECs) and mesenchymal stem cells (MSCs). These cells self-organized into 3-dimensional (3D) organoids, with HUVECs and MSCs localized centrally and underneath a layer of epithelial cells and PBGs. To generate a human multi-cellular BA model, we generated MBOs from the epithelial cells of BA patients (BA-MBOs). The BA-MBOs displayed markers of epithelial-mesenchymal transition (EMT) and upregulated transforming growth factor- β (TGF- β)/Activin-SMAD2/3 pathway without immune microenvironments. The importance of EMT and TGF- β in regulating the defects of the diseased epithelium was supported by a decrease in EMT and further maturation of epithelial cells upon blocking of TGF- β signaling in MBOs, and by a decreased biliary injury and fibrosis in neonatal mice treated with a TGF- β inhibitor.

Results

Cellular compartmentalization and formation of PBG-like structure in MBOs

Normal bile duct development and regeneration requires an interaction of liver progenitor epithelial cells with neighboring mesenchymal and endothelial cells^{21–23}. When cholangiocyte organoids are derived from human livers, they form spheroids comprised of epithelial cells without identifiable PBGs¹⁹. Here, we investigated the regulatory role of non-epithelial cells in the development of the biliary epithelium and PBGs, and in the delayed epithelial maturation associated with BA. First, we dissociated normal cholangiocyte organoids and cocultured them with HUVECs and human MSCs (Fig. 1a)^{24,25}. The mixture of three cell types was seeded on basement membrane extract matrix and incubated with an expansion media (EM)²⁶ containing R-spondin 1, EGF, FGF10, TGF- β inhibitor A8301, HGF, Forskolin, Gastrin and an equal proportion of endothelial cell growth medium (EGM)^{27,28} for 5 days. This was followed by culture in a cholangiocyte differentiation media (DM)²⁹ containing R-spondin 1, EGF, FGF2, DKK1, Forskolin and Dexamethasone with equal proportion of EGM for 9 days. A separate group of cholangiocytes was subjected to the same culture conditions (type of media and number of days in culture) to serve as controls (Supplementary Table 1). Cholangiocytes cultured in the presence of HUVECs and MSCs self-organized into 3D MBOs containing a central cell cluster juxtaposed to an outer cell layer. The outer cell layer organized in MBOs grew by 4-fold between 5 and 10 days of culture (Fig. 1b). In contrast, cholangiocytes plated as a single cell type grew as mono-lineage organoids (termed “Mono” to reflect the epithelium-only compartment) and formed spheroids (Fig. 1c, Supplementary Movie 1).

Immunostaining of MBOs revealed that the central cell cluster consisted of CD31 (also known as PECAMI) positive HUVECs and vimentin (VIM) positive MSCs. HUVECs maintained CD34 expression, which is a pattern previously described in portal vein endothelial cells

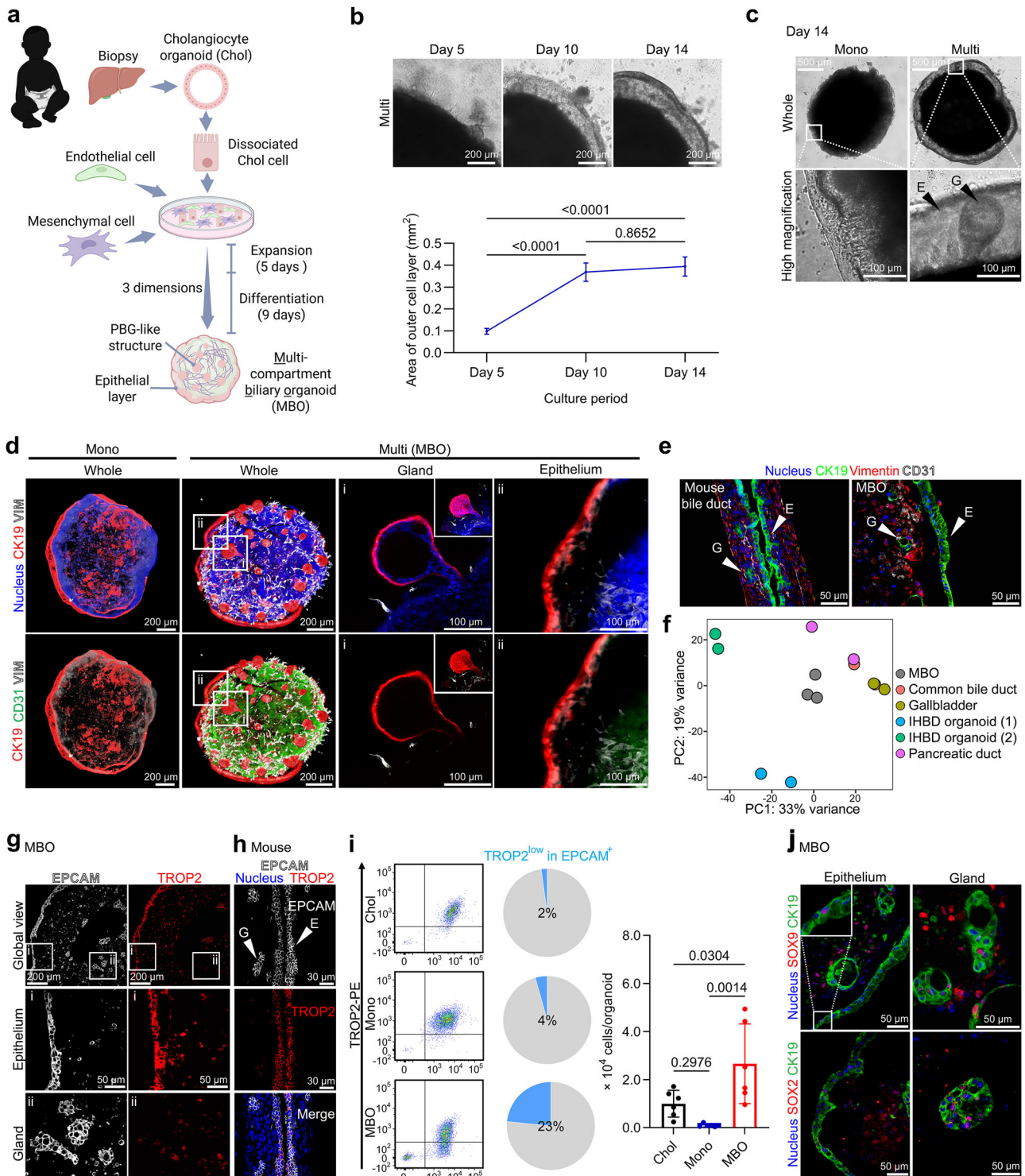
(Supplementary Fig. 1a)³⁰. For MSCs, the reduced expression of CD105 within MBOs supports a potential adaptation of MSCs to a hepatobiliary-like microenvironment of MBOs (Supplementary Fig. 1b)³¹. CK19 (also known as KRT19) positive cholangiocytes formed an outer cell layer and PBG-like structures embedded within the mesenchymal and endothelial cells, resembling the anatomic organization of bile duct tissue with PBGs (Fig. 1d, e). To gather insight into the transcriptional phenotype of MBO cells, we applied principal component analysis (PCA) to MBOs and published data curated from biliary tissues, and found that the MBOs are positioned away from cholangiocyte organoids and in proximity to common bile duct, gall bladder, and pancreatic duct tissues (Fig. 1f)³². Further immunostaining with antibodies against trophoblast surface protein 2 (TROP2 [also known as TACSTD2]) stained the epithelial layer uniformly, while PBGs lacked TROP2 signal or stained faintly^{33,34}, with both epithelial compartments expressing epithelial cell adhesion molecule (EPCAM) (Fig. 1g). This pattern was similar to the TROP2 immunostaining of mouse extrahepatic bile ducts (EHBD), as additional evidence that the differential expression of TROP2 in the MBO epithelium supported the epithelial compartmentalization and the presence of PBG compartments (Fig. 1g, h). By fluorescence activated cell sorting (FACS), the number of PBG epithelial cells (TROP2^{low}/EPCAM⁺) were \sim 2.7 and \sim 30-fold higher in a MBO compared to cholangiocytes prior to culture (“Chol”) and the mono-lineage (“Mono”) organoid group (Fig. 1i). Consistent with a property of housing stem cells⁴, PBG-like structures expressed the biliary tree stem/progenitor cell markers SOX9 and SOX2 (Fig. 1j)³⁵, and low level of LGR5 (Supplementary Fig. 1c)³⁶. Functional biliary differentiation in NC-MBO was supported by the expression of CFTR, ASBT [also known as SLC10A2] and AE2 [also known as SLC4A2]^{4,37} which was detected in a smaller frequency in epithelial cells of BA-MBOs (Supplementary Fig. 2a).

To identify the role of each cell type in MBO formation, we examined the co-culture outcome of different combinations of the three cell types. The co-culture of cholangiocytes with MSCs (without HUVECs) self-assembled into a distinct central cluster of MSCs and an adjacent but separate epithelial cell population. This formation differed from the distribution of MSCs of MBOs, which joined HUVECs to form subepithelial cell populations with direct contact with the epithelium. Co-culturing cholangiocytes and HUVECs (without MSCs) failed to form organoids (Supplementary Fig. 2b, c). Altogether, these results suggest that the culture of cholangiocytes with HUVECs and MSCs forms a suitable microenvironment for the development of epithelial cells and PBG-like structures, thus reproducing the two epithelial cellular compartments of bile ducts.

Modeling human BA using patient-derived MBOs

We next investigated the mechanisms underlying pathogenesis of BA by coculturing HUVECs and MSCs with cholangiocyte organoid cells derived from liver biopsies of BA patients (BA-MBOs). BA-MBOs self-organized similarly to MBOs from normal control donors (NC-MBO) but had incomplete epithelial lining (Fig. 2a, b and Supplementary Fig. 3a).

To investigate if epithelial cells of BA-MBOs displayed cell polarity defects^{19,20}, we first stained MBOs with anti-ZO1 (also known as TJP1) and anti- β -catenin antibodies (polarity markers). BA-MBOs displayed an aberrant staining pattern when compared to NC-MBOs (Fig. 2c). In addition, epithelial markers (CFTR, ASBT [also known as SLC10A2] and AE2 [also known as SLC4A2])^{4,37} and acetylated tubulin (cilium protein) were predominantly stained in the epithelial layer of NC-MBOs, with decreased expression in BA-MBOs (Supplementary Figs. 2a and 3b). Using the ratio of Alcian Blue⁺ to CK19⁺ epithelium to evaluate the excretory ability of acidic mucin, NC-MBOs had strong staining in PBGs of MBO, with nearly absent signal in BA-MBOs (Fig. 2d). These findings provide evidence that the delayed maturation affects PBGs, in addition to the epithelial defects previously reported in BA. Despite these



differences, the number of CK19⁺ cells expressing Ki67 or the of CK19 colocalized with cleaved caspase-3, surrogate markers of proliferation and apoptosis respectively, was similarly low in NC- and BA-MBOs (Supplementary Fig. 3c, d).

To examine the effects of long-term culture, we extended the culture of MBOs to 28 days. At this juncture, 3D rendering of images captured by confocal microscopy revealed that the structural integrity of NC-MBOs was preserved, with further growth of epithelial cells and PBGs juxtaposed to mesenchymal and endothelial cells. Although BA-MBOs also maintained anatomical organization with incomplete epithelial layer and rudimentary cells clusters resembling minute PBGs, these organoids had an expansion of VIM⁺ cells and a 3-fold reduction

of epithelial cell volume (Supplementary Fig. 3e). These observations underscore the feasibility of extended MBO culture, highlight the persistent epithelial anomalies in BA-MBOs, and reveal an accentuated fibrotic phenotype, which typically characterizes disease progression in affected children.

EMT in patient-derived organoids

To investigate the molecular basis of the abnormal epithelial development, we analyzed differentially expressed genes (DEGs) from RNA-seq and identified distinct transcriptional signatures showing increased expression of genes encoding matrix metalloproteinase 7 (*MMP-7* [also known as *MMP7*]) and osteopontin (*OPN* [also known as

Fig. 1 | Cellular compartmentalization and formation of PBG-like structure in MBOs. **a** Overview of MBO generation. Created in BioRender. Ayabe, H. (2025) <https://BioRender.com/iy9dzsm>. **b** Change in area of outer cell layer in MBOs from days 5-14 in culture (Mean \pm SEM, $n = 30$ organoids, Multi: NC-MBO). **c** Phase contrast images of biliary organoids (Mono: NC-MBO without HUVEC and MSC, G: gland-like structure, E: epithelium-like structure). Three experiments were repeated with similar results. **d** Whole-mount immunostaining of CK19 (red), CD31 (green), VIM (white) and nucleus (blue; Hoechst 33342) in MBOs. Three experiments were repeated with similar results. **e** Immunostaining of CK19 (green), CD31 (white), VIM (red) and nucleus (blue; DAPI) in 3-day-old mouse extrahepatic bile duct (left) and MBO (right). G: Gland-like structure and E: Epithelium. Three experiments were repeated with similar results. **f** PCA of MBO transcriptional

phenotype. RNA-sequencing data from MBOs were integrated into publicly available data³². The IHBD organoids were cultured in medium according to Huch et al. (1)²⁶ or extrahepatic medium (2)³². **g, h** Immunostaining of EPCAM (white) and TROP2 (red) in MBOs ($n = 3$) in **(g)** and EPCAM (white), TROP2 (red) and nucleus (blue; DAPI) in 3 to 4-day-old mouse extrahepatic bile ducts ($n = 3$) in **(h)**. G: Peribiliary gland and E: Luminal epithelium. **i** FACS of biliary organoids. Left: Representative plot for TROP2⁺/EPCAM⁺ and TROP2^{low}/EPCAM⁺ cells. Middle: Frequency of TROP2^{low} cells in EPCAM⁺ cells in MBOs ($n = 6$ organoids). Right: Number of TROP2^{low}/EPCAM⁺ cells in each group (Mean \pm SD, $n = 6$ organoids). **j** Immunostaining of SOX9 (red), SOX2 (red), CK19 (green) and nucleus (blue; DAPI) in MBOs ($n = 3$). **b, i** the p -values were shown in plots and were determined using one-way ANOVA with Tukey's test.

SPPI1), which play important roles in epithelial injury and the accentuated fibrosis of BA (Fig. 2e)^{38,39}. By immunohistochemical staining, MMP-7 and OPN expression was limited to the epithelial lining in NC-MBOs, while in BA-MBOs the staining was more intense in cells immediately adjacent to the thin epithelial lining (Fig. 2f). Based on these findings and on the role of endothelial and mesenchymal cells influencing bile duct development and pathogenesis of disease⁴⁰⁻⁴³, we tested the hypothesis that epithelial cells of BA-MBOs display EMT. First, to examine if the development of MBOs involves EMT, we compared the baseline expression level of VIM by pan-cytokeratin (pan-CK) positive cells in NC-MBOs and NC-Monos (Supplementary Table 1) by FACS. MBOs had a significant increase in pan-CK⁺/VIM⁺ cells (Fig. 2g). Next, we investigated degree of EMT in patient-derived MBOs.

To determine if EMT is preferentially increased in BA-MBOs, we first queried the RNAseq data from NC- and BA-MBOs using Gene Ontology (GO) and Molecular Signatures Database (MSigDB)^{44,45}. EMT signatures were enriched in the GO (*TGF β -3* [also known as *TGFB3*], *SNAI1*, *GREM1*) and MSigDB (*INHBA*, *OPN*, *GREM1*) results, in addition to TGF- β binding and receptor signaling, extracellular matrix (ECM), and collagen functions (Fig. 3a, b and Supplementary Data 1)⁴⁶, with the simultaneous increase of *TGF β -3*, *SNAI1* and *GREM1* in BA-MBO pointing to TGF- β pathway activation^{47,48}. In NC-MBOs, TGF- β 3 expression was detected primarily in the immediate subepithelial compartment, which increased by 4-fold in BA-MBO (Fig. 3c). Additional immunostaining for DESMIN (DES), a MSC marker⁴⁹, detected a similar pattern of DES⁺/CK19⁻ cells in both MBO groups, while percentage of CK19 overlapping with DES was increased in BA-MBOs (Supplementary Fig. 4a). Furthermore, immunostaining to evaluate for EMT showed increased expression of *SNAI1*, and *ZEB2* in CK19⁺ cells in BA-MBOs, with a decrease in epithelial co-staining for E-cadherin and CK19 (ECAD⁺/CK19⁺ cells) (Supplementary Fig. 4b)^{47,50}.

To determine the EMT temporal dynamics during organoid formation, we quantified VIM⁺ and pan-CK⁺ cells using FACS. After 5 days of culture, no changes were observed between NC- and BA-MBOs. At 14 days, pan-CK⁺/VIM⁺ hybrid cells (transitional state or partial EMT⁴³) were -2-fold higher, pan-CK⁻/VIM⁺ mesenchymal cells were -5-fold higher and pan-CK⁺/VIM⁻ epithelial cells (cholangiocytes) were -3-fold lower in BA-MBO compared to NC-MBO (Fig. 3d). Despite these changes in epithelial and mesenchymal cells, the population of endothelial cells was similar in NC- and BA-MBOs, as evidenced by whole-mount immunostaining using anti-CD31 and CK19 antibodies. Examining confocal images of organoids with the Imaris Filament Tracer Tool, both MBO groups contained cells forming short endothelial networks (Supplementary Fig. 4c).

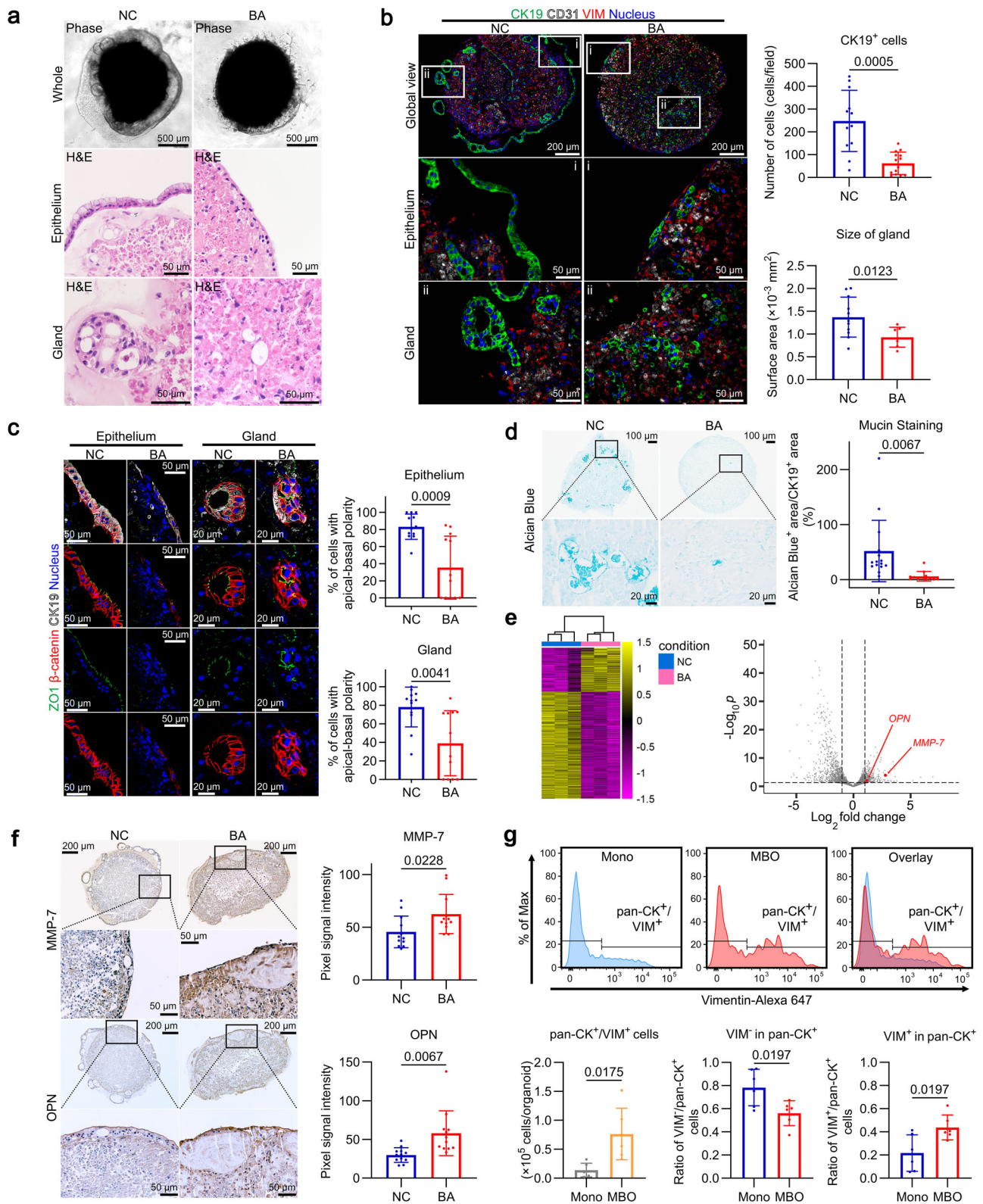
Cellular lineage of EMT in patient-derived organoids

To investigate the cell lineage of EMT, we performed single-cell RNA sequencing (scRNAseq) for MBOs. Transcriptome analysis of 27,645 cells identified 3 distinct primary cell clusters that predominantly expressed features of epithelial (*KRT7*, *KRT8*, *KRT19*, *EPCAM*), endothelial (*PTX3*, *CDCA2*, *ANKRD37*, *PGF*) and mesenchymal cells (*FNI*, *VIM*,

TFPI2), 5 smaller clusters representing intermediate populations, and 1 other cluster showing indeterminate identity (*SIOO4A*, *CD74*, *ARHG-DIB*, *HLA-DRA*, *IFI27*) (Fig. 3e, Supplementary Data 2). To initially visualize these intermediate cell populations, we used intensity-based co-localization analysis for percentage of CK19 signal overlapping with VIM signal. Using these markers, we localized these cells predominantly in BA-MBOs, where they populated the sites near the defective epithelium and in the subepithelial space (interspaced among mesenchymal and endothelial cells) (Supplementary Fig. 5a).

Among these Intermediate clusters (Fig. 3f and Supplementary Fig. 5b), intermediate cell groups 1, 2 and 4 were enriched for EMT genes, and Intermediate 1 included partial EMT or transitory cholangiocyte genes (e.g., *COL7A1*, *VEGFA*, *PDGFRB*, *COL6A3* and *ZEB2*), representing a subpopulation of epithelial cells with high mesenchymal potential. Intermediate 2 contained cells expressing mediator genes implicated in TGF- β -induced EMT (e.g., *LGALS1*, *IGFBP7*, *TAGLN*, *SPARC* and *ZEB1*), and cells in Intermediate 4 expressed ECM remodeling genes involved in TGF- β -induced EMT (e.g., *LOX*, *FNI*, *TGFB1*, *MMP2*, *SERPINE1*, *COL1A2*, *COL3A1*, *SPARC*, *INHBA*, *TGFB1*) (Supplementary Data 2 and 3). Cells in Intermediate clusters 2 and 4 were significantly over-represented in BA-MBOs relative to NC-MBOs (Fig. 3g). BA-MBOs also demonstrated an increased prevalence of cells scoring highly for top EMT-associated genes when compared to their normal control counterparts (Fig. 3h, and Supplementary Fig. 5c)⁵¹. Moreover, cell-cell interaction prediction identified that both NC and BA-MBOs had TGF- β ligand-receptor interactions (e.g., *TGF- β 1*, *INHBA* and *INHBB*) in Intermediate 1 and 4, but only BA-MBOs had this same interaction in the Intermediate 2 population (Supplementary Fig. 6a, b).

Since MBOs showed an upregulation of genes related to TGF- β -induced EMT and ECM remodeling, we assessed the activation of fibrosis in different cell types and calculated ECM scores using an extracellular matrix gene list including ECM glycoproteins, collagens, and proteoglycans from GSEA⁵². This approach identified populations of mesenchymal and intermediate cells with higher ECM scores and high correlation with EMT scores ($r = 0.934$, $p < 0.0001$), especially in BA-MBOs (Fig. 4a-c). To further investigate the temporal dynamics of the mesenchymal cell population in MBOs, we quantified MBO cells using FACS at days 5 and 14. Pan-CK⁺/VIM⁺ hybrid cells and pan-CK⁻/VIM⁺ mesenchymal cells increased in BA-MBOs (Fig. 4d, e). Measuring the surface area of organoids at day 14, BA-MBOs had a modest decrease in size compared to NC-MBO (Fig. 4f), potentially indicating a contraction by the expanded population of Intermediate and Mesenchymal cells (Fig. 4f). These findings suggest that there is activation of EMT-related ECM substrates in the expanding mesenchyme and intermediate populations of BA-MBOs (Fig. 4c). To examine a potential role of endothelial cells in organoid structure and its potential influence on the abnormal phenotype of BA-MBOs, we performed ligand-receptor analysis using scRNAseq. The endothelial cell cluster had 25 interactions involving VEGF ligands⁵³⁻⁵⁵ in NC-MBOs and 27 interactions in BA-MBOs. Visualization of these interactions inferred



strong crosstalk implicated in VEGF signals in Mesenchymal, Epithelial, Endothelial, and Intermediate cell clusters 1, 3, and 4, with similar patterns observed in both NC and BA-MBOs. Conversely, no relevant VEGF interaction was detected in Intermediate clusters 2, 5, and Other (Supplementary Table 2).

Altogether, these data identify phenotypic and transcriptional evidence of EMT in cell sub-populations. Additionally, the prominent signature of TGF- β /Activin-SMAD2/3 genes in intermediate clusters is

consistent with its function in biliary development, remodeling, and injury^{56–59}, and may regulate crosstalk between neighboring cells in the diseased tissue.

EMT suppresses epithelial maturation via TGF- β signaling

To directly determine if TGF- β signaling regulates EMT in BA, we cultured MBOs in A8301, a TGF- β inhibitor (Fig. 5a). In this experiment, the control groups were cultured for 5 days in EM/EGM (containing 2.5 μ M

Fig. 2 | Modeling human BA using patient-derived MBOs. **a** Phase contrast and H&E staining of NC- and BA-MBOs. Three experiments were repeated with similar results. **b** Immunostaining of CK19 (green), CD31 (white), VIM (red) and Nucleus (blue; DAPI) in MBOs. Abundance of CK19⁺ cells ($n = 12$ fields for NC or 14 fields for BA examined over 3 independent samples) and average size of gland-like structures ($n = 11$ fields for NC or 7 fields for BA examined over 3 independent samples) were quantified (Mean \pm SD). **c** Immunostaining of ZO1 (green), β -catenin (red), CK19 (white) and nucleus (blue; DAPI) in MBOs. Graphs show CK19⁺ cells exhibiting apical-basal polarity (Mean \pm SD; $n = 12$ fields per 3 organoids). **d** Alcian Blue staining for MBOs. Mucin production in epithelium was determined by ratio of

Alcian Blue⁺ areas in CK19⁺ (from separately examined immunofluorescence data) areas (Mean \pm SD; $n = 15$ fields [for NC] or 12 fields [for BA] examined over 3 independent samples). **e** Heatmap (left) and Volcano plot (right) of differentially expressed genes between NC- and BA-MBOs (up in BA: 350; down in BA: 851). **f** DAB staining of MBOs for MMP-7 and OPN. The staining intensities were quantified by imaging analysis (Mean \pm SD; $n = 12$ fields per 3 organoids). **g** Representative plots and quantification of FACS for hybrid cells (pan-CK⁺/VIM⁺) and cholangiocytes (pan-CK⁻/VIM⁺) in Mono and MBO. The number and cell ratio were quantified (Mean \pm SD; $n = 6$). For **b–d, f, g**, the p -values were shown in plots and were determined using two-tailed Welch's t -test.

A8301⁶⁰, followed by 9 days in DM/EGM (with DMSO and no A8301), while the experimental group of BA-MBO was under the same culture conditions containing a higher concentration of 10 μ M A8301 throughout the 0- and 9-day periods. A8301 decreased the number of pan-CK⁺/VIM⁺ hybrid cells in BA-MBOs and increased pan-CK⁻/VIM⁺ cholangiocytes without changing the number of pan-CK⁻/VIM⁺ cells (Fig. 5b). The use of a higher concentration of A8301 (100 μ M A8301) in separate experiments showed that the treatment reduced pan-CK⁺/VIM⁺ hybrid cells and pan-CK⁻/VIM⁺ mesenchymal cells, but did not increase pan-CK⁻/VIM⁺ cholangiocytes (Supplementary Fig. 6c–e). 3D rendering of whole-mount stained MBOs showed that A8301 restored the epithelial composition in BA-MBOs and formed a surface area of similar dimension of NC-MBOs. In addition, PBGs were easily identified and had similar size NC-MBOs (Fig. 5c). TGF- β inhibition also corrected epithelial defects of BA-MBOs, shown by a 2.9-fold increase in the percentage of ECAD⁺ cells compared to vehicle-treated BA-MBOs, and significantly improved the percent of ZO1⁺ cells and mucin production (Fig. 5d–f). We subsequently investigated the impact of including A8301 in the EM/EGM expansion medium during the initial five days at a concentration of 2.5 μ M on the culture of BA-MBOs. Omitting A8301 during this period did not significantly affect the volume of cholangiocytes and mesenchyme in BA-MBOs, nor the colocalization ratio of CK19 and VIM (Supplementary Fig. 7a, 7b). Altogether, these data show that the inhibition of TGF- β /Activin signaling reduced EMT in BA-MBOs and allowed for epithelial differentiation and expansion.

Next, we analyzed serum samples from BA patients at the time of diagnosis using large-scale proteomics data reported by our group previously³⁸; serum from age-matched healthy subjects served as control samples (normal controls or NC). We found a prominent EMT signature in the serum of BA patients using MSigDB hallmark 2020 gene set (including INHBA, TGFBI, TIMP1), in addition to inflammation (CXCL6, CXCL8 and CCL5) and ECM (COL23A1, LAMA1 and BGN) using GO terms (Fig. 5g and Supplementary Data 4). The heatmap generated by the EMT hit genes distinctly divided the serum samples into two clusters of NC and BA (Fig. 5h). Analyzing the expression of each TGF- β /Activin ligand on EMT in BA patients, we found that TGF- β 1, TGF- β 2, TGF- β 3 and INHBA expression levels were significantly increased above normal controls (Fig. 5i). Next, we directly investigated the relevance of this pathway by inhibiting TGF- β signaling in a mouse model of experimental biliary atresia.

Inhibition of TGF- β signaling decreases biliary injury and liver fibrosis in experimental BA

To determine if TGF- β -dependent EMT regulates epithelial injury in experimental BA, we infected BALB/c mice with Rhesus rotavirus (RRV) within 24 hours of birth; phosphate buffered saline was injected in control mice (Fig. 6a)^{10–12}. Analysis of extrahepatic bile ducts (EHBDs) by immunostaining showed that the percent of TGF- β 1⁺/CK19⁺ cells and TGF- β 3⁺/CK19⁺ cells increased -3.8 and -1.8-fold, respectively, above controls 7 days after RRV infection (time of biliary epithelial injury and duct obstruction) (Supplementary Fig. 7c, d). Then, we repeated the experiments and administered A8301 (1 mg/kg body

weight) intraperitoneally daily beginning 1 day after infection with RRV; phosphate-buffered saline was injected in a separate group of control mice. A8301 injections reduced the percentage of RRV-infected mice with jaundice, promoted long-term survival, and decreased serum bilirubin and alanine aminotransferase (Fig. 6b–e). Histologically, the biliary epithelium of EHBDs was largely intact, with a mild subepithelial inflammation. In liver sections, portal spaces had mild expansion, which contrasted to the full expression of the BA phenotype in untreated mice (Fig. 6f). Tissue staining for EMT showed that the coexistences of ECAD or CK19 and VIM induced by RRV infection was suppressed by A8301 (Fig. 6g). Applying a similar strategy to a neonatal mouse model of chronic hepatitis induced by a delayed infection of RRV⁶¹, we found that A8301 suppressed the development of cholestasis, liver and biliary injury, and hepatic fibrosis (Fig. 6h–m). Altogether, the rescue of the BA phenotypes by TGF- β inhibition point to a key role of the TGF- β pathway in pathogenesis of experimental BA.

To further examine the expression of TGF- β signaling in human liver biopsies, we immunostaining histological sections for TGF- β 1 and TGF- β 3 from BA patients. The percent of TGF- β 1⁺/CK19⁺ cells and TGF- β 3⁺/CK19⁺ increased -5.3 and -11-fold in BA patients (Fig. 6n and Supplementary Fig. 8a). Analysis of liver gene expression data (GSE46995; reported by our group previously⁶²) showed increased expression of SMAD2/3 pathway ligands of *TGFBI*, *TGFBI2*, *TGFBI3*, and the receptor of *TGFBR1*^{63–67} in BA patients when compared to liver biopsies from normal subjects (NC) or from patients with intrahepatic cholestasis (IHC; diseased control) (Supplementary Fig. 8b, c, and Supplementary Data 5). Using gene set enrichment analysis, EMT emerged as the most enriched term from the MSigDB hallmark set in genes upregulated in BA patients compared to NC and IHC (Supplementary Fig. 8d). Searching for evidence of EMT in BA livers, we immunostained histological sections for CK19 and VIM. The percent of VIM⁺/CK19⁺ cells was -1.8-fold higher in human BA (Fig. 6n). Altogether, these data indicate that the EMT signature and TGF- β expression identified in diseased biliary epithelium of MBOs are also detected in tissues of BA patients.

Discussion

Our study reveals that the co-culture of biliary epithelial cells with endothelial and mesenchymal cells leads to the spontaneous self-organization into an organoid exhibiting an epithelial layer with peribiliary glands embedded within a subepithelial compartment with endothelial and mesenchymal cells. This arrangement replicates the dual compartment of the biliary epithelium, thus forming a more comprehensive multi-lineage system to enable studies that take into account molecular processes and signals that more closely approaches the complexity of the human biliary system. In patient-derived BA-MBOs, the epithelium was fragmented and PBGs were small, had abnormal intercellular junction (ZO1 expression), and expressed markers of EMT, with a prominent expression of TGF- β 3. Upon TGF- β inhibition, EMT decreased in the diseased epithelium, the population of PBGs increased, and ZO1 expression improved. In vivo, TGF- β inhibition suppressed the BA phenotype and substantially decreased liver fibrosis in neonatal mice. These data point to a regulatory role of

Fig. 3 | Presence and cellular lineage of EMT in patient-derived organoids. **a** Top enriched terms of MSigDB Hallmark 2020^{45,79} and GO sets^{44,78} in genes upregulated in BA-MBOs vs NC-MBOs (MF: Molecular Function, BP: Biological Process, $n = 3$ organoids). **b** Boxplot visualization of EMT-related gene expressions in MBOs ($n = 3$ organoids). The box shows median, 25th and 75th percentile values and the whiskers show 1.5 IQR from the edges of the box. **c** DAB staining of MBOs for TGF- β 3. The staining intensities were quantified by imaging analysis (Mean \pm SD; $n = 12$ fields per 3 organoids). **d** Representative plots and quantification of FACS of day 5 and 14 MBOs. Number of cholangiocytes (pan-CK⁺/VIM⁺), hybrid cells (pan-CK⁺/VIM⁺) and

mesenchymal cells (pan-CK⁺/VIM⁺) in MBOs were quantified (Mean \pm SD, $n = 6$ organoids). **e** UMAP plots of scRNAseq for MBOs colored by cell type ($n = 4$ organoids). **f** Top 5 enriched terms (plus ties) of MSigDB Hallmark 2020 sets in genes upregulated in Intermediate clusters ($n = 4$ organoids). **g** Percent cell proportions of each cluster in MBOs ($n = 4$ organoids). The box shows median, 25th and 75th percentile values and the whiskers show the furthest point that is within 1.5 IQR from the edges of the box. The outliers are plotted outside the whiskers. **h** EMT score overlaid in the UMAP plot ($n = 4$ organoids). The p -values were shown in plots and were determined using DESeq2 model (**b**) and two-tailed Welch's t -test (**c**, **d**, **g**).

affected patients, which showed abnormal remodeling of hilar ducts, active fibroplasia, and attempts to renew the epithelium^{69–71}. The emergence of PBGs and epithelial expansion after EMT suppression via inhibition of TGF- β signaling highlights the significance of coordinated cellular diversity in epithelial development and the potential reversibility of EMT in disease states.

EMT plays a role in physiologic tissue remodeling and in regulating the fibrosis of multiple organs^{43,72}. Staining of EMT markers and FACS in NC-MBOs showed evidence of EMT in epithelial cells with anatomical and population features of cholangiocytes, suggesting continued normal remodeling at day 14. A potential cellular source emerged from scRNAseq of NC- and BA-MBOs, which identified the Intermediate 1, 2 and 4 clusters containing transcriptional enrichment of ECM-related genes on a variety of levels. ECM and EMT create feedback loops which can be regulated by TGF- β signaling^{46,73–75}. Future analysis of the transcriptional program uniquely upregulated in these intermediate clusters, such as *VIM*, *SNAI1*, *SNAI2*, *ZEB2* and *FNI*, may give insight into the molecular circuitry driving EMT and the developmental delay in epithelial and glandular in diseased states.

The engineering of multilineage human biliary organoids to study epithelial development elucidates an interplay between epithelial cells and their non-epithelial neighbors, underscoring the pivotal role of endothelial and mesenchymal cells in the formation and maintenance of epithelial and glandular structures within the bile duct. This MBO formation occurs despite the fact that MSCs and HUVECs are not derived from livers. Given the specificity of the niche cells in the liver, with different mesenchymal and endothelial subtypes specializing in their functions in vivo, MBOs therefore may not fully recapitulate the full phenotype of cell populations of the liver. Using patient-derived MBOs and virus infection of neonatal mice to model human BA, we demonstrate how disruptions in this interplay, particularly through TGF- β -dependent EMT, contribute to delayed development and lead to epithelium pathology and tissue fibrosis. In rotavirus-infected mice, residual tissue inflammation likely stems from the persistent activation of TGF- β -independent circuits triggered by rotavirus infection, which are mediated by tissue macrophages, dendritic cells, lymphocytes, and NK cells⁷. This notwithstanding, the effectiveness of TGF- β inhibition in suppressing EMT markers and improving the epithelial and glandular architecture points to a critical role of TGF- β in the pathogenesis of BA and as a potential therapeutic target. Our study also identifies areas of future research to fully elucidate the molecular mechanisms governing epithelial crosstalk with neighboring mesenchymal and endothelial cells during tissue development and disease states.

Methods

Human biopsy samples

Patients were recruited sequentially as they visited at a center in the consortium, which comprises of 15 centers. Human samples were obtained after informed consent from patients' parents/legal guardians. All procedures involving the use of human specimens were approved by the Research Ethics Committees at Cincinnati Children's Hospital Medical Center (CCHMC). Liver biopsy fragments used to generate cholangiocyte organoids were obtained from male and female subjects younger than 18 years of age, as follows: 9 from BA

patients ($n = 3$ at diagnosis, ages: 5 weeks to 2 months; and $n = 6$ at the time of transplantation, ages: 6 months to 2 years of age), and 6 from normal deceased donors (one of which had urea cycle defect; ages: 6 months to 17 years of age). Liver tissues used in histological analysis were from male and female pediatric subjects with BA ($n = 3$, ages: 8 months to 7 years of age) and normal deceased donors ($n = 3$, ages: 13–17 years of age). Demographic information was unavailable for one normal liver transplant donor (Supplementary Table 3).

Animals

BALB/c mice used for the studies were obtained from Charles River Laboratories. Mice were housed in the animal vivarium with a 12-hour dark-light cycle and ad libitum access to normal diet and water at CCHMC in accordance with the guidelines recommended by the Institutional Animal Care and Use Committee (IACUC; Protocol IACUC2020-0006).

Mesenchymal cells and endothelial cells

Human mesenchymal stem cells (MSCs) and human umbilical vein endothelial cells (HUVECs) were kindly gifted by Dr. Akihiro Asai (CCHMC) and cultured in mesenchymal stem cell growth medium (MSCGM; Lonza, PT-3001) and endothelial cell growth medium (EGM; Lonza, CC-3124).

Cholangiocyte organoids

Cholangiocyte organoids were generated from human liver tissues^{19,26}. Minced human liver tissues were washed in ice-cold basal medium containing Advanced Dulbecco's Modified Eagle Medium (DMEM)/F12 (Thermo Fisher Scientific, 12634028) supplemented with 100 U/ml Penicillin/Streptomycin (Thermo Fisher Scientific, 15140122), 1% GlutaMAX (Thermo Fisher Scientific, 35050061), and 10 mM HEPES (Thermo Fisher Scientific, 15630080). Tissue fragments were suspended in Cultrex Reduced Growth Factor Basement Membrane Extract Type 2 Pathclear (BME; Bio-Techne, 3533-005-02) and plated into 24 well plates as a 50 μ L droplet/well. After incubating at 37 °C to solidify, the tissue domes were initially cultured using 500 μ L/well of Isolation Medium (IM) containing basal medium supplemented with 1 \times B27 Supplement minus vitamin A (Thermo Fisher Scientific, 12587010), 1 \times N-2 Supplement (Thermo Fisher Scientific, 17502048), 1 mM N-acetylcysteine (Sigma-Aldrich, A7250), 10% vol/vol homemade R-spondin 1 conditioned media¹⁹, 10 mM Nicotinamide (Sigma-Aldrich, N0636), 10 nM Recombinant human Gastrin (Sigma-Aldrich, G9145), 50 ng/ml recombinant human Epidermal Growth Factor (EGF; Pepro-Tech, AF100-15), 100 ng/ml recombinant human Fibroblast Growth Factor 10 (FGF10; PeproTech, 100-26), 25 ng/ml recombinant human Hepatocyte Growth Factor (HGF; PeproTech, 100-39H), 10 μ M Forskolin (Bio-Techne, 1099), 5 μ M A 83-01 (Sigma-Aldrich, SML0788), 25 ng/ml recombinant human Noggin (Bio-Techne, 6057-NG), 30% vol/vol homemade Wnt Family Member 3A (WNT3A) conditioned medium¹⁹, and 10 μ M Y-27632 (Bio-Techne, 1254) for 5 days. IM was then replaced with Expansion Medium (EM) consisting of IM without Noggin, WNT3A and Y-27632. After reaching high density, the generated organoids were mechanically dissociated into small fragments and transferred to new plates.

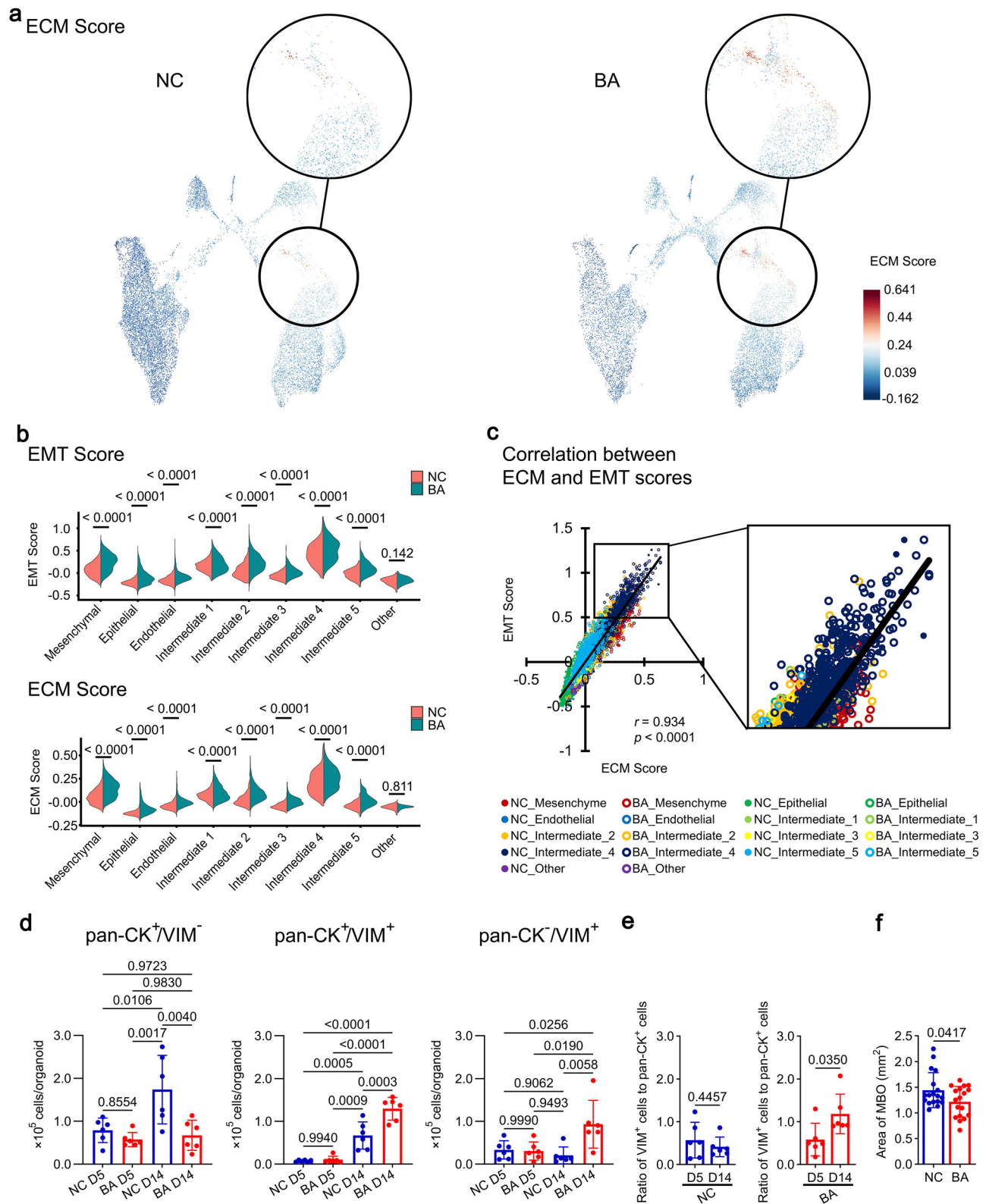


Fig. 4 | Analysis of MSC and EMT-expressing populations in MBOs. a ECM score overlaid in the UMAP plot ($n = 4$ organoids). **b** Violin plots showing EMT (upper) and ECM (lower) scores in clusters of NC- and BA-MBOs ($n = 4$ organoids). Source Data file contains exact p -values for comparison between cell types. **c** Scatter plot showing correlation between EMT and ECM scores ($n = 8$ organoids). The circles were filled by test groups and colored by clusters. **d** MBO cell number kinetics by FACS at days 5 and 14, with graphs showing numbers of cholangiocytes (pan-CK⁺/VIM⁻), hybrid cells (pan-CK⁺/VIM⁺) and mesenchymal cells (pan-CK⁻/VIM⁺) in each

MBO (mean \pm SD, $n = 6$ organoids). **e** Ratios of VIM⁺ cells to pan-CK⁺ cells in MBOs on day 5 and 14. VIM⁺ cells were divided by pan-CK⁺ cells (mean \pm SD, $n = 6$ organoids). **f** Surface area of MBOs at day 14 in culture (Mean \pm SD, $n = 18$ organoids). The p -values were shown in plots and were determined using two-tailed Wilcoxon rank sum test with Benjamini–Hochberg correction (**b**), `cor.test` function in R, which utilizes an asymptotic t approximation (**c**), one-way ANOVA with Tukey's test (**d**), and two-tailed Welch's t -test (**e**, **f**). Two-tailed Spearman's correlation test was used to assess the relationship between EMT and ECM scores (**c**).

Fig. 5 | TGF- β -induced EMT is a candidate regulator of BA phenotypes.

a Overview of in vitro A8301-mediated TGF- β signal inhibition in BA-MBOs. Created in BioRender. Ayabe, H. (2025) <https://BioRender.com/q1pk62z>. **b** Representative plots and quantification of FACS of day 14 MBOs treated with A8301. Number of hybrid (pan-CK⁺/VIM⁺), cholangiocyte (pan-CK⁺/VIM⁻) and mesenchymal (pan-CK⁻/VIM⁺) cells were quantified (Mean \pm SD; $n = 12$ organoids). **c** Images of MBOs treated with A8301 captured before collection and after whole-mount immunostaining (CK19: red, CD31: green, VIM: white). Abundance of CK19⁺ structures (Mean \pm SD; $n = 9$ organoids examined over 3 independent experiments) and size distribution of PBG-like structures were quantified ($n = 39$ –104 clusters examined over 3 independent experiments). **d** Immunostaining of ECAD (green), CK19 (red) and Nucleus (blue; DAPI) in MBOs treated with A8301. ECAD⁺ cells in CK19⁺ cells in the field were quantified (Mean \pm SD; $n = 12$ fields from 3 organoids). **e** Immunostaining of ZOI

(green), CK19 (red) and Nucleus (blue; DAPI) in MBO treated with A8301. ZOI⁺ cells in CK19⁺ cells per field were quantified (Mean \pm SD; $n = 12$ fields from 3 organoids). **f** Alcian blue staining of MBOs treated with A8301. Mucin production was determined by ratio of Alcian Blue⁺ areas in CK19⁺ (from separately examined immunofluorescence data) areas (Mean \pm SD; $n = 12$ fields from 3 organoids). **g** Top enriched terms of MSigDB Hallmark 2020^{45,79} and GO^{44,78} sets in serum proteins (reanalyzed from Lertdomphonwanit et al.³⁸) upregulated in BA subjects ($n = 175$ patients) vs age-matched normal controls ($n = 9$). MF: Molecular Function, BP: Biological Process. **h** Heatmap of enriched proteins in the EMT pathway in MSigDB Hallmark 2020 sets. ($n = 9$ NC and 175 BA subjects). **i** Serum TGF- β /Activin ligand levels represented by the relative fluorescent unit (RFU; Mean \pm SD). ($n = 9$ NC and 175 BA subjects). The p -values were shown in plots and were determined using one-way ANOVA with Tukey's test (**b**–**f**) and two-tailed Welch's t -test (**i**).

G8644), 20 mM HEPES, 1% GlutaMax, 100 U/mL Penicillin/Streptomycin, 1% ITS+ Premix (Corning, 354352), 10 μ M Forskolin, 10 nM Dexamethasone (Bio-Techne, 1126), 10% vol/vol in-house R-spondin1 conditioned media, 20 ng/mL recombinant human EGF, 5 ng/mL recombinant human FGF basic (Bio-Techne, 233-FB), and recombinant human Dkk-1 protein (Bio-Techne, 5439-DK) in William's E medium (Thermo Fisher Scientific, 12551032). The cholangiocyte organoid cells in MBOs were collected from multiple human subjects, and the same MSCs and HUVECs were used throughout this study.

Cholangiocyte organoids were dissociated and phenotyped by FACS prior to being subjected to further culture (forming a group termed "Chol"). Dissociated 4.7×10^5 cholangiocytes were subjected to the same culture conditions (type of media and number of days in culture) to serve as a control group termed "Mono-lineage biliary organoid" (or "Mono") (Supplementary Table 1). Unless otherwise noted, all MBO experiments were performed on day 14 of culture. Images were captured using either a compound (Olympus, IX71) or stereo (Leica, M205A) microscope. CellSens (RRID: SCR_014551, Olympus) or Leica Application Suite (RRID: SCR_016555, Leica) were used for visualization. Image J/Fiji (RRID: SCR_002285)⁷⁶ was used for image quantification. Live imaging was performed using Celldiscover 7 (ZEISS) and visualized using ZEN software (RRID:SCR_013672, ZEISS).

Whole-mount immunostaining

MBOs were fixed in 4% paraformaldehyde (PFA; Electron Microscopy Sciences, 15710)/DPBS, followed by permeabilization with 4% PFA/0.5% Triton X-100 (Sigma-Aldrich, T9284)/DPBS and 0.1% Tween 20 (Fisher scientific, BP337)/DPBS. MBOs were, then, cleared using PEGASOS protocol⁷⁷. In brief, the MBOs were decolorized overnight with 25% Quadrol (Sigma-Aldrich, 122262)/5% Ammonium hydroxide (Fisher scientific, 423305000) and washed with DPBS. After washing, the MBOs were treated with blocking solution (5% normal donkey serum [Jackson ImmunoResearch, 017-000-121]/5% normal goat serum [Jackson ImmunoResearch, 005-000-121]/0.3% Triton X-100) at 4 °C overnight and incubated at 4 °C for 2 days with primary antibodies diluted in 1% Bovine Serum Albumin (Jackson ImmunoResearch, 001-000-162)/0.3% Triton X-100/DPBS. Samples were then incubated at 4 °C overnight with fluorescent dye-conjugated secondary antibodies followed by nuclear staining with Hoechst 33342 (Thermo Fisher Scientific, H1399). Specific antibody details are listed in the Supplementary Table 4 and Reporting summary. MBOs were sequentially delipidated using 30%, 50% and 70% tert-Butanol (tB; Sigma-Aldrich, 360538) solution containing 3% Quadrol and dehydrated with tB-PEG medium (75% tB/22% poly [ethylene glycol] methacrylate [PEGMMA; Sigma-Aldrich, 409529] and 3% Quadrol) for 1 day. The MBOs were finally treated with benzyl benzoate (BB; Sigma-Aldrich, B6630)-PEG clearing medium (75% BB/22% PEGMMA/3% Quadrol) until the tissue turned transparent. For cilia staining, MBOs were fixed in 4% PFA/DPBS and washed with DPBS, followed by permeabilization and blocking with 1% BSA/0.5% Triton X-100/DPBS (P/B buffer) at room temperature for 1 hour. MBOs were then incubated at 4 °C for 1 day with primary

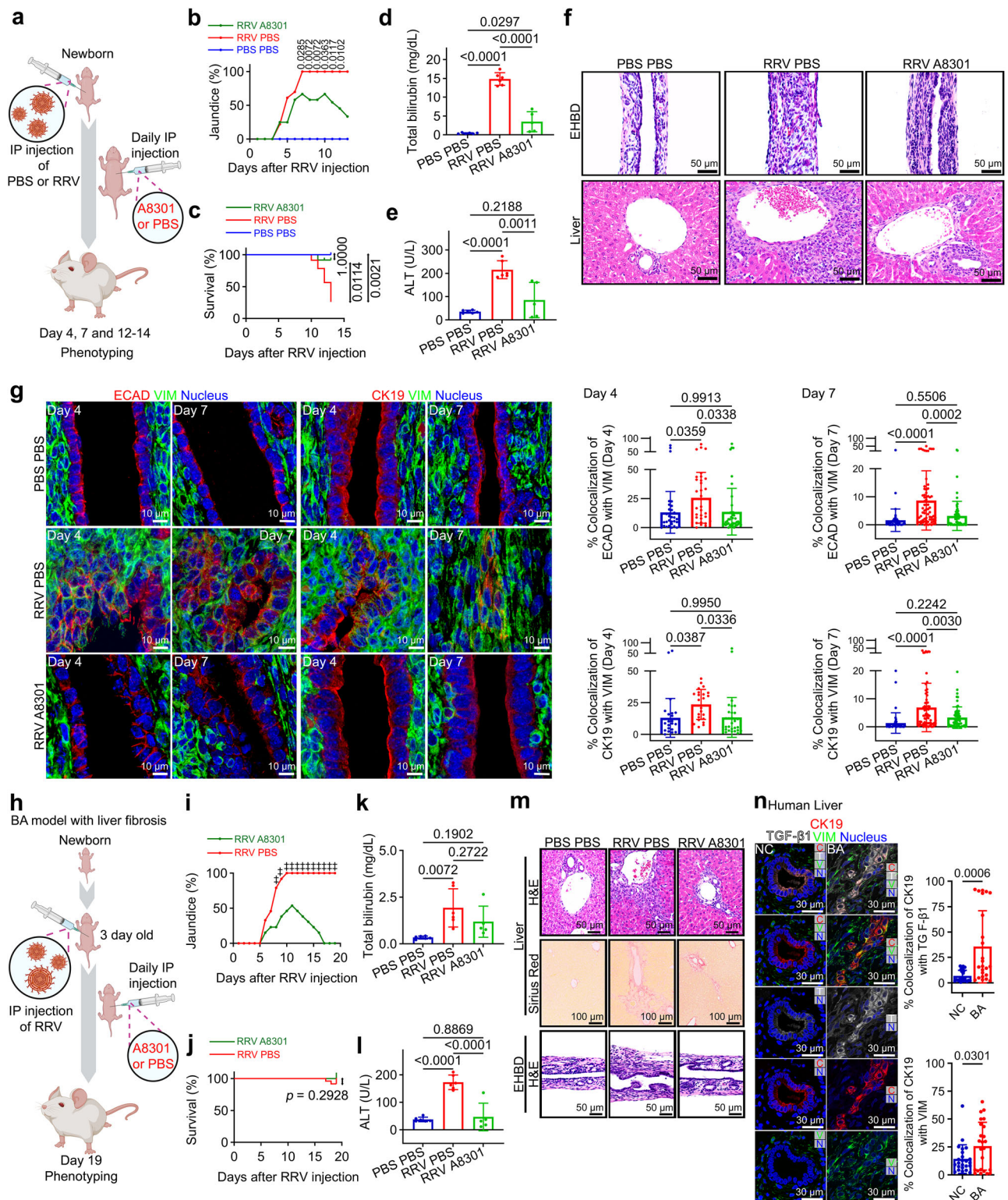
antibodies in P/B buffer and washed with 0.2% Triton X-100/DPBS. After washing, MBOs were incubated with fluorescent dye-conjugated secondary antibodies/Hoechst 33342 in P/B buffer at 4 °C overnight. Whole-mount immunofluorescence images were captured using confocal microscope (Nikon, ECLIPSE Ti; Zeiss, LSM880) and NIS Elements (RRID: SCR_014329, Nikon), Black Zen software (RRID:SCR_018163, Zeiss) and Imaris (RRID: SCR_007370, Oxford Instruments) were used for visualization and quantification of images.

FACS analysis

To obtain single cells, MBOs were washed several times with DPBS and dissociated as mentioned above. Dissociated cells were washed and passed through 40 μ m cell strainer and stained in DPBS using the Zombie Violet Fixable Viability Kit (BioLegend, 423113). Flow cytometry (FACS) buffer (DPBS/2% Fetal Bovine Serum [FBS; Thermo Fisher Scientific, 26140079]) was used for subsequent wash steps. For pan-CK⁺/VIM⁺ staining, cells were incubated with BUV395-conjugated CD31 antibody (BD Bioscience, 565290) and PerCP-Cy5.5-conjugated CD73 antibody (BD Bioscience, 561260), washed with FACS buffer and fixed in IC Fixation Buffer (Thermo Fisher Scientific, 00-8222). Fixed cells were subsequently washed with 1 \times permeabilization buffer (Thermo Fisher Scientific, 00-8333), followed by intracellular-staining with Alexa fluor 488-conjugated pan-CK (Thermo Fisher Scientific, 53-9003-82) and VIM antibodies (Abcam, ab92547) in 1 \times permeabilization buffer. Following washing, VIM-specific signals were obtained by incubation with Alexa fluor 647-conjugated anti-rabbit IgG antibody (Cell Signaling Technology, 4414). For TROP2⁺/EPCAM⁺ staining, cells were incubated with PE-conjugated TROP2 (BioLegend, 363804) and EPCAM antibodies (R and D Systems, AF960) in FACS buffer after the live/dead staining described above. After washing, EPCAM-specific signals were obtained using Alexa fluor 647-conjugated anti-goat IgG antibody (Jackson ImmunoResearch Labs, 705-605-147). Washed cells were subjected to FACS analysis using LSRFortessa Cell Analyzer (BD Bioscience). Appropriate single stains and fluorescence minus one (FMO) controls were also performed. Cells were sequentially gated based on size and granularity (forward scatter [FSC] versus side scatter [SSC]) and singlets (FSC-Area versus FSC-Height). Dead cells were excluded using Zombie Violet. Cholangiocytes (pan-CK⁺/VIM⁺), mesenchymal cells (pan-CK⁻/VIM⁺) and hybrid cells (pan-CK⁺/VIM⁺) were selected from CD31⁻ population. TROP2⁺ epithelial cells (TROP2⁺/EPCAM⁺) and TROP2⁻ epithelial cells (TROP2⁻/EPCAM⁺) were selected from EPCAM⁺ population (Supplementary Fig. 9, Supplementary Table 4 and Reporting summary). Data were analyzed using FlowJo (RRID: SCR_008520, BD Bioscience).

Experimental mouse BA models

For testing in vivo effects of TGF- β signal inhibition, we used two murine models. For modeling biliary injury and obstruction in BA, newborn BALB/c mice were intraperitoneally injected with 1.5×10^6 fluorescent-forming units (ffu) of RRV within 24 hours after birth (Fig. 6a)^{10,12}. To model liver fibrosis in BA, 3-day old BALB/c mice were intraperitoneally injected with 1.875×10^6 ffu of RRV (Fig. 6h)⁶¹. Mice



injected with DPBS were used as normal controls. To inhibit TGF-β signaling, 1 mg/kg of A8301 sodium (MedChemExpress, HY-10432A) in 20 μL of DPBS was injected intraperitoneally and daily beginning 6 hours after RRV inoculation. Mice were monitored daily for jaundice, body weight, and survival. EHBs and livers were harvested, and blood was collected with Microvette (Sarstedt, 16.444.100) to obtain plasma following IACUC-approved protocols. Plasma bilirubin and ALT were analyzed using Total Bilirubin Reagent Set (Pointe Scientific, B7538-

120) and DiscretPak ALT Reagent Kit (Catachem, V164-0A) and levels were quantified using a Synergy HI Hybrid Reader (BioTek).

Imaging histological staining and fluorescence

MBOs were collected in DPBS by manual pipetting, fixed in 4% PFA/DPBS at 4 °C overnight and placed in 70% ethanol at 4 °C after DPBS washings. Mouse EHBs and livers were fixed in 10% formalin (Fisher scientific, SF100-4) at room temperature. Routine paraffin embedding

Fig. 6 | Clinical relevance and therapeutic potential of TGF- β -induced EMT in BA. **a** RRV-induced BA mouse model with biliary injury (biliary-injury model). Newborn were injected intraperitoneally (IP) with PBS or RRV followed by daily PBS or A8301. Created in BioRender. Ayabe, H. (2025) <https://BioRender.com/b5mlrv9>. **b–e** Jaundice and survival rates ($n = 9$ control [PBS PBS]/23 BA [RRV PBS]/12 BA-treated [RRV A8301] mice), and total bilirubin and plasma ALT (mean \pm SD; $n = 6$ control/6 BA/5 BA-treated mice) in biliary injury model. **f** H&E-stained EHBD and liver from day 12–14 biliary-injury model. **g** Immunostaining of VIM (green), ECAD or CK19 (red) and Nucleus (blue; DAPI) in day-4 and day-7 biliary-injury model. VIM and ECAD or CK19 colocalization in control/BA/BA-treated mice were quantified (ECAD: $n = 32/32/41$ fields examined over 3 mice [day-4], $n = 48/69/60$ fields examined over 4 mice [day-7], CK19: $n = 24/23/31$ fields examined over 3 mice [day-4], $n = 49/66/60$ fields examined over 4 mice [day-7]) (mean \pm SD). **h** RRV-induced BA mouse model with liver fibrosis (fibrosis model). 3-day old mice were injected IP

with PBS or RRV followed by daily PBS or A8301. Created in BioRender. Ayabe, H. (2025) <https://BioRender.com/6fpm0xa>. **i–l** Jaundice and survival rates ($n = 24$ BA/13 BA-treated mice), total bilirubin and plasma ALT (mean \pm SD; $n = 6$ control/6 BA/5 BA-treated mice) in fibrosis model. **i** $p < 0.01$. Source Data file contains exact p -values. **m** Representative images of H&E-stained liver and EHBD ($n = 6$ control/8 BA/6 BA-treated mice) and Sirius Red-stained liver ($n = 6$ mice in each group). Experiments were repeated with similar results. **n** Tissue expression of TGF- β in human BA. Immunostaining of CK19 (C; red), TGF- β 1 (T; white), VIM (V; green) and DAPI (N; blue; nucleus) in a liver biopsy from BA patient. Graphs depict colocalization of CK19 and TGF- β 1 or VIM (mean \pm SD; $n = 24$ fields from 3 subjects). The p -values were shown in plots and were determined using two-tailed Fisher's exact test (**i**) with Bonferroni correction (**b**), Log-rank test (**j**) with Bonferroni correction (**c**), one-way ANOVA with Tukey's test (**d**, **e**, **g**, **k**, **l**) and two-tailed Welch's t -test (**n**).

and serial 5 μ m sectioning were performed at the Research Pathology core at CCHMC. Sections were baked at 60 $^{\circ}$ C and deparaffinized using Histo-Clear (National Diagnostics, HS-200), followed by re-hydrating with graded ethanol-water solutions. Heat-induced epitope-retrieval was performed using 1 \times Target Retrieval Solution pH 6.1 (Agilent, S1699) or 1 \times Target Retrieval Solution pH 9.0 (Agilent, S2367). For immunohistochemistry, sections were incubated in 3.0% hydrogen peroxide (Sigma-Aldrich, 216763) and stained with primary antibodies and an avidin-biotin complex kit (Vector Laboratories, PK-6101 or PK-4002) with peroxidase substrate (Vector Laboratories, SK-4100). For immunofluorescence, cells were washed in DPBS then fixed in 4% PFA and washed with DPBS. MSCs were permeabilized by 0.1% Triton X-100/DPBS and HUVECs by 0.2% Tween 20/DPBS. The permeabilized cells or antigen-retrieved sections were blocked using serum from the same host species as the secondary antibodies and incubated with primary antibodies diluted in Antibody diluent (Agilent, S0809), followed by secondary antibodies. Antifade mounting medium with DAPI (Thermo Fisher Scientific, P36931) was used for covering the slides. To detect human TROP2 and human EPCAM, mouse anti-human TROP2 antibody (DSHB, CPTC-TACSTD2-2) and goat anti-human EPCAM antibody (R and D Systems, AF960) were used. For mouse, goat anti-mouse TROP2 antibody (R and D systems, AF1122) and rat anti-mouse EPCAM antibody (BD Bioscience, 552370) were used. Specific antibody details are listed in the Supplementary Table 4 and Reporting Summary. Conventional Hematoxylin (Poly Scientific R&D, s212) & Eosin (Sigma-Aldrich, HT1101128) staining to characterize morphology, Alcain blue (Richard-Allan Scientific, 88043) to identify acidic mucin production, and Sirius red (Dudley Corporation, 74189) staining for evaluation of liver fibrosis were performed. Bright field images were captured using a light microscope (Olympus, BX43) and immunofluorescence images were captured using either fluorescence (Olympus, BX51; Nikon, ECLIPSE Ni-E) or confocal (Nikon, ECLIPSE Ti; Zeiss, LSM880) microscopes. Imaris and Image J/Fiji were used for visualization and quantification of images.

Image analysis

Whole-mount immunostaining images of MBOs were analyzed using Imaris (Oxford Instruments) software. Surface rendering objects of the red channel (CK19) were created by the Surface Creation Wizard to obtain epithelial cell volumes and PBG sizes. Total number and average surface area, length, and branching number of CD31 $^{+}$ green channel surfaces in MBOs were quantified using Imaris Filament Tracer Tool. Staining intensity level in the positive area of DAB staining was measured using ImageJ/Fiji software. Color deconvolution for DAB staining and hematoxylin were applied and mean grey values in the positive area were measured using the deconvoluted DAB images. Areas of images were measured using ImageJ/Fiji software and ratio of positive cell was quantified by counting the number of positive cells per CK19 $^{+}$ cells. Colocalization of immunostaining images were measured using the Coloc modules in Imaris software.

Library preparation and sequencing for bulk RNA-seq

MBOs were collected in TRIzol Reagent (Thermo Fisher Scientific, 15596026), subjected to total RNA extraction using miRNeasy Micro Kit (Qiagen, 217084) and verified for integrity by 2100 Bioanalyzer (Agilent, G2939BA). Total RNA was poly A selected and reverse-transcribed using TruSeq RNA library preparation kit V2 (Illumina, RS-122). Each sample was fitted with one of the 24 adapters containing a different 6 base molecular barcode for high level multiplexing. After 12 cycles of PCR amplification, completed libraries were sequenced on an Illumina NovaSeq 6000 (Illumina), generating around 20 million high quality 125 base-long reads per sample.

Data Processing for bulk RNA-seq

The quality assessment and pre-processing of MBO RNA-seq reads were performed using FASTQC (RRID:SCR_014583, version 0.11.2), Trim Galore (RRID:SCR_011847, version 0.4.2) with Cutadapt (RRID:SCR_011841, version 1.14), and SAMtools (RRID:SCR_002105, version 1.10.0). Reads were then aligned to hg38 genome using Bowtie2 (RRID:SCR_016368, version 2.3.3.1). Low-quality alignments and PCR duplicates were removed using SAMtools (version 1.10.0) and Picard MarkDuplicates tool (RRID:SCR_006525, version 2.18.22). Gene expression was quantified using htseq-count (RRID:SCR_011867, version 0.6.1).

Bulk RNA-seq analysis

Differential expression analysis was performed using Bioconductor DESeq2 package (RRID:SCR_015687, version 1.34.0) in R 4.1.2 (RRID:SCR_001905). Volcano plot visualization of the differential expression results was generated using Bioconductor EnhancedVolcano package (RRID:SCR_018931, version 1.12.0). Heatmap visualization of differentially expressed genes was generated using R pheatmap package (RRID:SCR_016418, version 1.0.12). Gene expression was normalized using DESeq2 variance stabilizing transformation and z-score scaled. For pathway enrichment analyses, overrepresentation of MSigDB Hallmark 2020 Genesets and GO terms in the upregulated genes in RNA-seq of BA vs. NC was tested using Enrichr (RRID:SCR_001575) and ToppGene (RRID:SCR_005726)^{44,45,78,79}. Genes with adjusted p value < 0.05 and log₂ fold change ≥ 1.00 were selected for the pathway enrichment analysis. Expression of EMT related genes in RNA-seq of BA-MBO vs NC-MBO was visualized with Boxplot. Gene expression values are represented as log₂-transformed DESeq2 normalized counts.

Principal component analysis (PCA) of bulk RNA-seq

Raw sequencing files of RNA-seq of in vivo tissues were downloaded from Rimland et al.³². Reads were pre-processed, aligned, and quantified using the same pipelines and reference genome as described for the MBO RNA-seq data. Gene expression in NC-MBO and in vivo tissue samples were normalized using DESeq2 variance stabilizing transformation. Batch differences between in vitro and in vivo samples were

corrected using the ComBat algorithm in the Bioconductor *sva* package (RRID:SCR_012836, version 3.42.0)⁸⁰. Principal component analysis (PCA) was performed using the PCA function in the FactoMineR package (RRID:SCR_014602, version 2.4) using the top 2000 most highly variable genes and visualized using the ggplot2 package (RRID:SCR_014601, version 3.3.6).

Library preparation and sequencing for single-cell RNA sequencing (scRNAseq)

To obtain single cells, MBOs were washed several times with DPBS and dissociated using Dissociation Buffer. The dissociated cells were passed through a 30 μ m cell strainer (pluriSelect, 43-50030-01) and resuspended in William's E medium containing 0.01% Bovine Serum Albumin (Sigma-Aldrich, A3059). ScRNAseq was performed according to the Chromium Single Cell 3' Reagent Kit v3.1 protocol (10 \times Genomics) with the Chromium platform (10 \times Genomics), aiming for 10,000 cells. The barcoded cDNA was cleaned with Silane DynaBeads and amplified using 14 PCR cycles. Full-length, barcoded cDNA was then enzymatically fragmented, sized-selected using SPRIselect Reagent, adapter-ligated, and amplified for library construction. During the library construction, the Illumina R2 primer sequence, paired-end constructs with P5 and P7 sequences, and sample indexes were added. The samples were pooled and run on the NovaSeq 6000 system sequencer (Illumina) using S4 flow cells and paired-end NovaSeq 6000 S4 Reagent Kit v1.5 (200 cycles) (Illumina, 20028313), aiming for a minimum of 325 M reads per sample.

Dataset Processing for scRNAseq

The raw sequencing data were processed using Cell Ranger (RRID:SCR_023221, version 6.0.0) to generate FASTQ files and counts matrices following standard practices. For quality control, each sample was subjected to a filter of 500 minimum UMIs detected, 250 minimum features detected, and less than 50% of features mapping to the mitochondrial genome. This resulted in 27,645 cells remaining for the 8 samples, of which 4 were NC-MBOs and 4 were BA-MBOs. The gene expression data were log normalized and scaled with Seurat (RRID:SCR_016341, v4.0.3) according to the authors recommendations. Following normalization and scaling, integration was done with Seurat to merge the samples into a unified dataset using 2000 integration features. Clustering was performed at a resolution of 0.5, which resulted in 15 original clusters. Dimensionality reduction TSNE and UMAP plots were generated for visualization purposes.

Cell classification

Differential expression was performed to identify genes unique to each of the clusters using default parameters for minimum fraction expression and log fold change threshold, which indicated the need to merge similar clusters due to few unique features. Expression of known marker genes from the literature and expert recommendations, together with Enrichr and ToppGene-based pathway analysis and scoring cells from reference signatures, were used to make the final classifications^{78,79}. Genes with adjusted *p* value < 0.05 and log₂ fold change > 1.00 were selected for the pathway enrichment analysis. Redundant, mature epithelial and mesenchymal clusters were each merged into single clusters, while the small immune-like population, the endothelial-like population, and each of the proposed epithelial-mesenchymal transition (EMT) populations were left separated. Due to the low cell number and low DEG number, one cluster was referred as "Other". This cluster expresses genes related to mesenchyme⁸¹, histocompatibility complex^{82,83} and EMT^{81,84}. However, CD45 (*PTPRC*)⁸⁵ is not included in the DEGs indicating that the cell in this cluster are not immune cells but cells having immune-like gene expression. Bar plots displaying differential proportions between normal control and biliary atresia organoids were generated using the ggplot2 package (version 3.4.4).

EMT and ECM scores

Identification of clusters along the EMT and ECM production was done by examining each cluster for high expression of the top 100 EMT-associated genes from the EMTome resource and the 275 ECM-related genes from core matrisome genes^{51,52}. To score cells for EMT and ECM activity, we adapted a previously described method for combined gene expression scoring⁸⁶. Briefly, each cell in the data set is scored based on the combined normalized expression of all genes in the provided signature. To do this, for each gene in the signature, the scoring function first defines a set of 100 control genes whose expression is similar to the provided gene. The average expression of the control genes is then subtracted from the expression of the signature gene per cell for normalization. The normalized values for all gene are then averaged to get an overall score for each cell in the dataset. To generate the UMAP plot, an array of colors is generated, ranging from the minimum score per dataset to the global maximum score, which allows for accurate visual comparison between datasets of different conditions. Code for reproducing this scoring can be found in the project GitHub repository in the code availability section.

Cell-cell interaction prediction

Receptor-ligand interactions were predicted using CellPhoneDB (RRID:SCR_017054) with default parameters⁸⁷. Chord diagrams were used to visualize the interactions between cell types in the NC-MBO and BA-MBO organoids separately with the circlize (RRID:SCR_002141, version 0.4.15) and chorddiag (version 0.1.3) packages in R⁸⁸.

Proteomics data

The data were downloaded from our previously published article (Lertudomphonwanit et al.³⁸). Briefly, serum proteins from a total of 175 BA subjects and age-matched normal controls (NC, *n* = 9) were measured by high-throughput proteomic assay (SOMAscan). Statistical analyses between the BA and NC groups were conducted using Student's *t* test with FDR correction (Benjamini-Hochberg procedure) using stats (version 4.1.0). Proteins with adjusted *p* value < 0.1 and log₂ fold change \geq 0.585 were selected for pathway enrichment analysis using Enrichr and ToppGene. Heatmap were generated using pheatmap (version 1.0.12) and employing log₂ transformed serum protein levels that were enriched in the EMT pathway in MSigDB Hallmark 2020 Gene sets. Serum TGF- β /Activin ligand levels were indicated using relative fluorescent unit (RFU).

Quantification and statistical analysis

For organoid culture experiments, quantifications were carried out at least by measuring 3 subjects per condition to increase reproducibility. For animal experiments, a minimum of three mice were included. Unless otherwise noted, GraphPad Prism 9 (RRID: SCR_002798, GraphPad Software) was used for all statistical analysis with two-tailed, an unpaired t-test for two group comparisons. In cases where more than two groups were being compared, one-way ANOVA was performed followed by Tukey's test. *p*-values of <0.05 were considered statistically significant.

For scRNAseq, the results were analyzed using two-tailed, unpaired Welch's t-test for two group comparisons in parametric data and non-parametric data were analyzed using Wilcoxon Rank Sum test. To analyze the relationship between EMT score and ECM score, Spearman's Rank Correlation test was used. Differential expression with at least a 2-fold change (apeglm shrinkage) and false discovery rate <0.05 was considered significant in bulk RNA-seq analysis. Data are represented as mean with standard deviation unless otherwise noted. In Enrichr and ToppGene analyses, the *p*-values were defined by Fisher's exact test and adjusted as *q*-values by Benjamini-Hochberg method. In the enrichment analysis of bulk-RNAseq, scRNAseq, and microarray data, genes with log₂ fold change greater than or equal to 1 and adjusted *p*-value less than 0.05 were considered differentially

expressed. In the enrichment analysis of proteomics data, to identify 76 DEGs, genes with log₂ fold change greater than or equal to 0.585 and adjusted *p*-value less than 0.1 were considered differentially expressed. Gene sets with less than 15 or more than 200 genes were not used for ToppGene analysis and the gene sets were selected using Enrichr analysis^{45,89}. The combined score is the z-score multiplied by the natural log of the *p*-value⁷⁹. The bubble plots were generated using Prism software. Details referring to the specific numbers of replicates for each experiment can be found in the figure legends.

Reporting summary

Further information on research design is available in the Nature Portfolio Reporting Summary linked to this article.

Data availability

All raw and processed RNA-Seq and scRNAseq data generated in this work are publicly available at the Gene Expression Omnibus (GEO) data repository under accession code GSE266169, [<https://www.ncbi.nlm.nih.gov/geo/query/acc.cgi?acc=GSE266169>] (subseries: GSE264201 and GSE264440). Previously published microarray, RNA-seq and proteomics data are available from the following sources: Bessho et al.⁶² (GSE46995 [<https://www.ncbi.nlm.nih.gov/geo/query/acc.cgi?acc=GSE46995>]), Rimland et al.³² (E-MTAB-7569 in EMBL-EBI [<https://www.ebi.ac.uk/biostudies/ArrayExpress/studies/E-MTAB-7569>]) and Lertudomphonwanit et al.³⁸ (which contain the source data [<https://www.science.org/doi/10.1126/scitranslmed.aan8462>]). Source data are provided with this paper.

Code availability

All original code has been deposited at Zenodo and is publicly available as of the date of publication (<https://doi.org/10.5281/zenodo.15556238>). Additionally, the code used to generate the data and figures presented in this paper can be found at the project's GitHub repository: <https://github.com/EDePasquale/Shivakumar-MBO>.

References

- Cardinale, V. et al. The biliary tree—a reservoir of multipotent stem cells. *Nat. Rev. Gastroenterol. Hepatol.* **9**, 231–240 (2012).
- Lemaigre, F. P. Development of the intrahepatic and extrahepatic biliary tract: a framework for understanding congenital diseases. *Annu. Rev. Pathol.* **15**, 1–22 (2020).
- Matsubara, T. et al. Peribiliary glands: development, dysfunction, related conditions and imaging findings. *Abdom. Radiol.* **45**, 416–436 (2020).
- de Jong, I. E. M., van Leeuwen, O. B., Lisman, T., Gouw, A. S. H. & Porte, R. J. Repopulating the biliary tree from the peribiliary glands. *Biochim. Biophys. Acta Mol. Basis Dis.* **1864**, 1524–1531 (2018).
- Lazaridis, K. N., Strazzabosco, M. & Larusso, N. F. The cholangiopathies: disorders of biliary epithelia. *Gastroenterology* **127**, 1565–1577 (2004).
- Maroni, L. et al. Functional and structural features of cholangiocytes in health and disease. *Cell Mol. Gastroenterol. Hepatol.* **1**, 368–380 (2015).
- Bezerra, J. A. et al. Biliary atresia: clinical and research challenges for the twenty-first century. *Hepatology* **68**, 1163–1173 (2018).
- Alagille, D. Extrahepatic biliary atresia. *Hepatology* **4**, 7S–10S (1984).
- Bezerra, J. A., Asai, A., Tiao, G., Mullapudi, B. & Balistreri, W. F. Biliary atresia and other disorders of the extrahepatic bile ducts. *Liver Dis. Child.* **5**, 162–181 (2021).
- Riepenhoff-Talty, M. et al. Group A rotaviruses produce extrahepatic biliary obstruction in orally inoculated newborn mice. *Pediatr. Res* **33**, 394–399 (1993).
- Petersen, C. et al. New aspects in a murine model for extrahepatic biliary atresia. *J. Pediatr. Surg.* **32**, 1190–1195 (1997).
- Shivakumar, P. et al. Preferential TNF α signaling via TNFR2 regulates epithelial injury and duct obstruction in experimental biliary atresia. *JCI Insight* **2**, e88747 (2017).
- Mack, C. L. What causes biliary atresia? Unique aspects of the neonatal immune system provide clues to disease pathogenesis. *Cell Mol. Gastroenterol. Hepatol.* **1**, 267–274 (2015).
- Harpavat, S., Finegold, M. J. & Karpen, S. J. Patients with biliary atresia have elevated direct/conjugated bilirubin levels shortly after birth. *Pediatrics* **128**, e1428–e1433 (2011).
- Harpavat, S. et al. Diagnostic yield of newborn screening for biliary atresia using direct or conjugated bilirubin measurements. *JAMA* **323**, 1141–1150 (2020).
- Berauer, J. P. et al. Identification of polycystic kidney disease 1 like 1 gene variants in children with biliary atresia splenic malformation syndrome. *Hepatology* **70**, 899–910 (2019).
- Lam, W. Y. et al. Identification of a wide spectrum of ciliary gene mutations in nonsyndromic biliary atresia patients implicates ciliary dysfunction as a novel disease mechanism. *EBioMedicine* **71**, 103530 (2021).
- Glessner, J. T. et al. Biliary atresia is associated with polygenic susceptibility in ciliogenesis and planar polarity effector genes. *J. Hepatol.* **79**, 1385–1395 (2023).
- Amarachintha, S. P. et al. Biliary organoids uncover delayed epithelial development and barrier function in biliary atresia. *Hepatology* **75**, 89–103 (2022).
- Babu, R. O. et al. Beta-amyloid deposition around hepatic bile ducts is a novel pathobiological and diagnostic feature of biliary atresia. *J. Hepatol.* **73**, 1391–1403 (2020).
- Strazzabosco, M. & Fabris, L. Development of the bile ducts: essentials for the clinical hepatologist. *J. Hepatol.* **56**, 1159–1170 (2012).
- Cordero-Espinoza, L. et al. Dynamic cell contacts between periportal mesenchyme and ductal epithelium act as a rheostat for liver cell proliferation. *Cell Stem Cell* **28**, 1907–1921 e1908 (2021).
- Gaudio, E. et al. Cholangiocytes and blood supply. *World J. Gastroenterol.* **12**, 3546–3552 (2006).
- Takebe, T. et al. Vascularized and functional human liver from an iPSC-derived organ bud transplant. *Nature* **499**, 481–484 (2013).
- Takebe, T. et al. Vascularized and complex organ buds from diverse tissues via mesenchymal cell-driven condensation. *Cell Stem Cell* **16**, 556–565 (2015).
- Huch, M. et al. Long-term culture of genome-stable bipotent stem cells from adult human liver. *Cell* **160**, 299–312 (2015).
- Camp, J. G. et al. Multilineage communication regulates human liver bud development from pluripotency. *Nature* **546**, 533–538 (2017).
- Ayabe, H. et al. Optimal hypoxia regulates human iPSC-derived liver bud differentiation through intercellular TGFB signaling. *Stem Cell Rep.* **11**, 306–316 (2018).
- Sampaziotis, F. et al. Reconstruction of the mouse extrahepatic biliary tree using primary human extrahepatic cholangiocyte organoids. *Nat. Med.* **23**, 954–963 (2017).
- Theuerkauf, I., Zhou, H. & Fischer, H. P. Immunohistochemical patterns of human liver sinusoids under different conditions of pathologic perfusion. *Virchows Arch.* **438**, 498–504 (2001).
- Kholodenko I. V., Kurbatov L. K., Kholodenko R. V., Manukyan G. V. & Yarygin K. N. Mesenchymal stem cells in the adult human liver: hype or hope? *Cells* **8**, 1127 (2019).
- Rimland, C. A. et al. Regional differences in human biliary tissues and corresponding in vitro-derived organoids. *Hepatology* **73**, 247–267 (2021).
- Matsui, S. et al. Characterization of peribiliary gland-constituting cells based on differential expression of trophoblast cell surface protein 2 in biliary tract. *Am. J. Pathol.* **188**, 2059–2073 (2018).

34. Fernandez Vallone, V. et al. Trop2 marks transient gastric fetal epithelium and adult regenerating cells after epithelial damage. *Development* **143**, 1452–1463 (2016).
35. Lanzoni, G., Cardinale, V. & Carpino, G. The hepatic, biliary, and pancreatic network of stem/progenitor cell niches in humans: a new reference frame for disease and regeneration. *Hepatology* **64**, 277–286 (2016).
36. Singh, S. et al. Heterogeneous murine peribiliary glands orchestrate compartmentalized epithelial renewal. *Dev. Cell* **58**, 2732–2745 e2735 (2023).
37. Claro da Silva, T., Polli, J. E. & Swaan, P. W. The solute carrier family 10 (SLC10): beyond bile acid transport. *Mol. Asp. Med.* **34**, 252–269 (2013).
38. Lertudomphonwanit C. et al. Large-scale proteomics identifies MMP-7 as a sentinel of epithelial injury and of biliary atresia. *Sci. Transl. Med.* **9**, eaan8462 (2017).
39. Kong, M., Ma, T. & Xiang, B. ANKRD1 and SPP1 as diagnostic markers and correlated with immune infiltration in biliary atresia. *Medicine* **100**, e28197 (2021).
40. Sakaguchi, T. F., Sadler, K. C., Crosnier, C. & Stainier, D. Y. Endothelial signals modulate hepatocyte apicobasal polarization in zebrafish. *Curr. Biol.* **18**, 1565–1571 (2008).
41. Gordillo, M., Evans, T. & Gouon-Evans, V. Orchestrating liver development. *Development* **142**, 2094–2108 (2015).
42. Wallace, S. J., Tacke, F., Schwabe, R. F. & Henderson, N. C. Understanding the cellular interactome of non-alcoholic fatty liver disease. *JHEP Rep.* **4**, 100524 (2022).
43. Lambert, A. W. & Weinberg, R. A. Linking EMT programmes to normal and neoplastic epithelial stem cells. *Nat. Rev. Cancer* **21**, 325–338 (2021).
44. Ashburner, M. et al. Gene ontology: tool for the unification of biology. The Gene Ontology Consortium. *Nat. Genet* **25**, 25–29 (2000).
45. Liberzon, A. et al. The molecular signatures database (MSigDB) hallmark gene set collection. *Cell Syst.* **1**, 417–425 (2015).
46. Scott, L. E., Weinberg, S. H. & Lemmon, C. A. Mechanochemical signaling of the extracellular matrix in epithelial-mesenchymal transition. *Front Cell Dev. Biol.* **7**, 135 (2019).
47. Xu, J., Lamouille, S. & Derynck, R. TGF-beta-induced epithelial to mesenchymal transition. *Cell Res* **19**, 156–172 (2009).
48. Hong, D. et al. Gremlin1 delivered by mesenchymal stromal cells promoted epithelial-mesenchymal transition in human esophageal squamous cell carcinoma. *Cell Physiol. Biochem* **47**, 1785–1799 (2018).
49. Au, P., Tam, J., Fukumura, D. & Jain, R. K. Bone marrow-derived mesenchymal stem cells facilitate engineering of long-lasting functional vasculature. *Blood* **111**, 4551–4558 (2008).
50. Cano, A. et al. The transcription factor snail controls epithelial-mesenchymal transitions by repressing E-cadherin expression. *Nat. Cell Biol.* **2**, 76–83 (2000).
51. Vasaikar, S. V. et al. EMTome: a resource for pan-cancer analysis of epithelial-mesenchymal transition genes and signatures. *Br. J. Cancer* **124**, 259–269 (2021).
52. Naba, A. et al. The extracellular matrix: tools and insights for the “omics” era. *Matrix Biol.* **49**, 10–24 (2016).
53. Ferrara, N., Gerber, H. P. & LeCouter, J. The biology of VEGF and its receptors. *Nat. Med.* **9**, 669–676 (2003).
54. Koch, S. & Claesson-Welsh, L. Signal transduction by vascular endothelial growth factor receptors. *Cold Spring Harb. Perspect. Med.* **2**, a006502 (2012).
55. Olsson, A. K., Dimberg, A., Kreuger, J. & Claesson-Welsh, L. VEGF receptor signalling - in control of vascular function. *Nat. Rev. Mol. Cell Biol.* **7**, 359–371 (2006).
56. Chung-Davidson, Y. W. et al. TGF-beta Signaling Plays a Pivotal Role During Developmental Biliary Atresia in Sea Lamprey (*Petromyzon marinus*). *Hepatol. Commun.* **4**, 219–234 (2020).
57. Harada, K. et al. Epithelial-mesenchymal transition induced by biliary innate immunity contributes to the sclerosing cholangiopathy of biliary atresia. *J. Pathol.* **217**, 654–664 (2009).
58. Clotman, F. et al. Control of liver cell fate decision by a gradient of TGF beta signaling modulated by Onecut transcription factors. *Genes Dev.* **19**, 1849–1854 (2005).
59. Lovisa, S. et al. Epithelial-to-mesenchymal transition induces cell cycle arrest and parenchymal damage in renal fibrosis. *Nat. Med.* **21**, 998–1009 (2015).
60. Tojo, M. et al. The ALK-5 inhibitor A-83-01 inhibits Smad signaling and epithelial-to-mesenchymal transition by transforming growth factor-beta. *Cancer Sci.* **96**, 791–800 (2005).
61. Luo, Z., Shivakumar, P., Mourya, R., Gutta, S. & Bezerra, J. A. Gene expression signatures associated with survival times of pediatric patients with biliary atresia identify potential therapeutic agents. *Gastroenterology* **157**, 1138–1152.e1114 (2019).
62. Bessho, K. et al. Gene expression signature for biliary atresia and a role for interleukin-8 in pathogenesis of experimental disease. *Hepatology* **60**, 211–223 (2014).
63. Yadin, D., Knaus, P. & Mueller, T. D. Structural insights into BMP receptors: Specificity, activation and inhibition. *Cytokine Growth Factor Rev.* **27**, 13–34 (2016).
64. Wakefield, L. M. & Hill, C. S. Beyond TGFbeta: roles of other TGFbeta superfamily members in cancer. *Nat. Rev. Cancer* **13**, 328–341 (2013).
65. Mueller, T. D. & Nickel, J. Promiscuity and specificity in BMP receptor activation. *FEBS Lett.* **586**, 1846–1859 (2012).
66. Allendorph, G. P., Isaacs, M. J., Kawakami, Y., Izipisua Belmonte, J. C. & Choe, S. BMP-3 and BMP-6 structures illuminate the nature of binding specificity with receptors. *Biochemistry* **46**, 12238–12247 (2007).
67. Peng, J. et al. Growth differentiation factor 9: bone morphogenetic protein 15 heterodimers are potent regulators of ovarian functions. *Proc. Natl. Acad. Sci. USA* **110**, E776–E785 (2013).
68. Hayata, Y. et al. Axin2 (+) peribiliary glands in the periampullary region generate biliary epithelial stem cells that give rise to ampullary carcinoma. *Gastroenterology* **160**, 2133–2148 e2136 (2021).
69. Balistreri, W. F. et al. Biliary atresia: current concepts and research directions. Summary of a symposium. *Hepatology* **23**, 1682–1692 (1996).
70. Bove, K. E. et al. Inflammation, active fibroplasia, and end-stage fibrosis in 172 biliary atresia remnants correlate poorly with age at kasai portoenterostomy, visceral heterotaxy, and outcome. *Am. J. Surg. Pathol.* **42**, 1625–1635 (2018).
71. Tan, C. E., Driver, M., Howard, E. R. & Moscoso, G. J. Extra-hepatic biliary atresia: a first-trimester event? Clues from light microscopy and immunohistochemistry. *J. Pediatr. Surg.* **29**, 808–814 (1994).
72. Lopez-Novoa, J. M. & Nieto, M. A. Inflammation and EMT: an alliance towards organ fibrosis and cancer progression. *EMBO Mol. Med.* **1**, 303–314 (2009).
73. Kasai, H., Allen, J. T., Mason, R. M., Kamimura, T. & Zhang, Z. TGF-beta1 induces human alveolar epithelial to mesenchymal cell transition (EMT). *Respir. Res.* **6**, 56 (2005).
74. Massague, J. & Sheppard, D. TGF-beta signaling in health and disease. *Cell* **186**, 4007–4037 (2023).
75. Shintani, Y., Maeda, M., Chaika, N., Johnson, K. R. & Wheelock, M. J. Collagen I promotes epithelial-to-mesenchymal transition in lung cancer cells via transforming growth factor-beta signaling. *Am. J. Respir. Cell Mol. Biol.* **38**, 95–104 (2008).
76. Schindelin, J. et al. Fiji: an open-source platform for biological-image analysis. *Nat. Methods* **9**, 676–682 (2012).
77. Jing, D. et al. Tissue clearing of both hard and soft tissue organs with the PEGASOS method. *Cell Res.* **28**, 803–818 (2018).

78. Chen, J., Bardes, E. E., Aronow, B. J. & Jegga, A. G. ToppGene Suite for gene list enrichment analysis and candidate gene prioritization. *Nucleic Acids Res.* **37**, W305–W311 (2009).
79. Chen, E. Y. et al. Enrichr: interactive and collaborative HTML5 gene list enrichment analysis tool. *BMC Bioinform.* **14**, 128 (2013).
80. Johnson, W. E., Li, C. & Rabinovic, A. Adjusting batch effects in microarray expression data using empirical Bayes methods. *Bio-statistics* **8**, 118–127 (2007).
81. Vongwiwatana, A., Tasanarong, A., Rayner, D. C., Melk, A. & Halloran, P. F. Epithelial to mesenchymal transition during late deterioration of human kidney transplants: the role of tubular cells in fibrogenesis. *Am. J. Transplant.* **5**, 1367–1374 (2005).
82. Spierings, E. Minor histocompatibility antigens: past, present, and future. *Tissue Antigens* **84**, 374–360 (2014).
83. Shiina, T., Hosomichi, K., Inoko, H. & Kulski, J. K. The HLA genomic loci map: expression, interaction, diversity and disease. *J. Hum. Genet.* **54**, 15–39 (2009).
84. Li, S. et al. Interferon alpha-inducible protein 27 promotes epithelial-mesenchymal transition and induces ovarian tumor-igenicity and stemness. *J. Surg. Res.* **193**, 255–264 (2015).
85. Hermiston, M. L. et al. Differential impact of the CD45 juxtamembrane wedge on central and peripheral T cell receptor responses. *Proc. Natl. Acad. Sci. USA* **106**, 546–551 (2009).
86. Griffin, G. K. et al. Ultraviolet radiation shapes dendritic cell leukaemia transformation in the skin. *Nature* **618**, 834–841 (2023).
87. Efremova, M., Vento-Tormo, M., Teichmann, S. A. & Vento-Tormo, R. CellPhoneDB: inferring cell-cell communication from combined expression of multi-subunit ligand-receptor complexes. *Nat. Protoc.* **15**, 1484–1506 (2020).
88. Flor M. chorddiag: create a D3 chord diagram. GitHub repository, package version 0.1.3. (2015).
89. Reimand, J. et al. Pathway enrichment analysis and visualization of omics data using g:Profiler, GSEA, Cytoscape and EnrichmentMap. *Nat. Protoc.* **14**, 482–517 (2019).

Acknowledgements

The authors acknowledge the support from Dr. Li Yang, Dr. Akihiro Asai, the Single Cell Genomics Facility (Kelly Rangel, Shawn Smith, RRID: SCR_022655), DNA Sequencing and Genotyping Core, and the Clinical Component of the Digestive Health Center at Cincinnati Children's Hospital Medical Center. We would also like to thank UT Southwestern Quantitative Light Microscopy Core Facility. Figures 1a, 5a, 6a, h and Supplementary Fig. 6c and 7a were created with BioRender.com. The Zeiss LSM880 confocal system was supported by a grant (1S10OD021684-01) to Katherine Luby-Phelps. This research was supported by grants from the NIH, DK 64008 and DK 83781 (J.A.B.).

Author contributions

Conceptualization, H.A., P.S., and J.A.B.; methodology, H.A., E.A.K.D., P.S., and J.A.B.; formal analysis, H.A., E.A.K.D., and W.L.; investigation, H.A. and E.A.K.D.; resources, H.A., S.P.A., S.N., S.R.F., K.K., P.S., and J.A.B.; writing—original draft, H.A., R.M., P.S., and J.A.B.; writing, review & editing, all authors; visualization, H.A., E.A.K.D., and W.L.; supervision, P.S. and J.A.B.; funding acquisition, J.A.B.

Competing interests

The authors declare no competing interests.

Additional information

Supplementary information The online version contains supplementary material available at <https://doi.org/10.1038/s41467-025-61442-5>.

Correspondence and requests for materials should be addressed to Pranavkumar Shivakumar or Jorge A. Bezerra.

Peer review information *Nature Communications* thanks the anonymous reviewers for their contribution to the peer review of this work. A peer review file is available.

Reprints and permissions information is available at <http://www.nature.com/reprints>

Publisher's note Springer Nature remains neutral with regard to jurisdictional claims in published maps and institutional affiliations.

Open Access This article is licensed under a Creative Commons Attribution-NonCommercial-NoDerivatives 4.0 International License, which permits any non-commercial use, sharing, distribution and reproduction in any medium or format, as long as you give appropriate credit to the original author(s) and the source, provide a link to the Creative Commons licence, and indicate if you modified the licensed material. You do not have permission under this licence to share adapted material derived from this article or parts of it. The images or other third party material in this article are included in the article's Creative Commons licence, unless indicated otherwise in a credit line to the material. If material is not included in the article's Creative Commons licence and your intended use is not permitted by statutory regulation or exceeds the permitted use, you will need to obtain permission directly from the copyright holder. To view a copy of this licence, visit <http://creativecommons.org/licenses/by-nc-nd/4.0/>.

© The Author(s) 2025